

Alma Mater Studiorum Università di Bologna  
Archivio istituzionale della ricerca

Mechanical Reliability of Fullerene/Tin Oxide Interfaces in Monolithic Perovskite/Silicon Tandem Cells

This is the final peer-reviewed author's accepted manuscript (postprint) of the following publication:

*Published Version:*

De Bastiani M., Armaroli G., Jalmoor R., Ferlauto L., Li X., Tao R., et al. (2022). Mechanical Reliability of Fullerene/Tin Oxide Interfaces in Monolithic Perovskite/Silicon Tandem Cells. ACS ENERGY LETTERS, 7(2), 827-833 [10.1021/acseenergylett.1c02148].

*Availability:*

This version is available at: <https://hdl.handle.net/11585/858231> since: 2022-02-14

*Published:*

DOI: <http://doi.org/10.1021/acseenergylett.1c02148>

*Terms of use:*

Some rights reserved. The terms and conditions for the reuse of this version of the manuscript are specified in the publishing policy. For all terms of use and more information see the publisher's website.

This item was downloaded from IRIS Università di Bologna (<https://cris.unibo.it/>).  
When citing, please refer to the published version.

(Article begins on next page)

This is the final peer-reviewed accepted manuscript of:

Michele De Bastiani, Giovanni Armaroli, Rawan Jalmoood, Laura Ferlauto, Xiaole Li, Ran Tao, George T. Harrison, Mathan K. Eswaran, Randi Azmi, Maxime Babics, Anand S. Subbiah, Erkan Aydin, Thomas G. Allen, Craig Combe, Tobias Cramer, Derya Baran, Udo Schwingenschlögl, Gilles Lubineau, Daniela Cavalcoli, and Stefaan De Wolf, *Mechanical Reliability of Fullerene/Tin Oxide Interfaces in Monolithic Perovskite/Silicon Tandem Cells*, ACS Energy Letters 2022 7 (2), 827-833.

The final published version is available online at:  
<https://doi.org/10.1021/acseenergylett.1c02148>

Rights / License:

The terms and conditions for the reuse of this version of the manuscript are specified in the publishing policy. For all terms of use and more information see the publisher's website.

This item was downloaded from IRIS Università di Bologna (<https://cris.unibo.it/>)

**When citing, please refer to the published version.**

# Mechanical Reliability of Fullerene/Tin Oxide Interfaces in Monolithic Perovskite/Silicon Tandem Cells

Michele De Bastiani,\* Giovanni Armaroli, Rawan Jalmoor, Laura Ferlauto, Xiaole Li, Ran Tao, George T. Harrison, Mathan K. Eswaran, Randi Azmi, Maxime Babics, Anand S. Subbiah, Erkan Aydin, Thomas G. Allen, Craig Combe, Tobias Cramer, Derya Baran, Udo Schwingenschlögl, Gilles Lubineau, Daniela Cavalcoli, and Stefaan De Wolf\*



Cite This: <https://doi.org/10.1021/acsnenergylett.1c02148>



Read Online

ACCESS |



Metrics & More

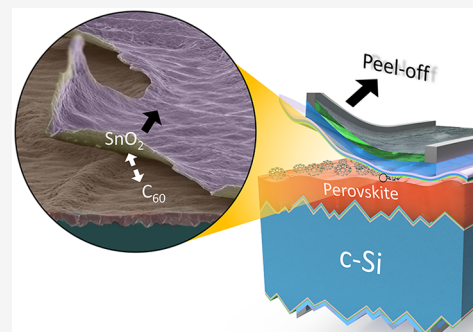


Article Recommendations



Supporting Information

**ABSTRACT:** High-efficiency perovskite-based solar cells comprise sophisticated stacks of materials which, however, often feature different thermal expansion coefficients and are only weakly bonded at their interfaces. This may raise concerns over delamination in such devices, jeopardizing their long-term stability and commercial viability. Here, we investigate the root causes of catastrophic top-contact delamination we observed in state-of-the-art *p-i-n* perovskite/silicon tandem solar cells. By combining macroscopic and microscopic analyses, we identify the interface between the fullerene electron transport layer and the tin oxide buffer layer at the origin of such delamination. Specifically, we find that the perovskite morphology and its roughness play a significant role in the microscopic adhesion of the top layers, as well as the film processing conditions, particularly the deposition temperature and the sputtering power. Our findings mandate the search for new interfacial linking strategies to enable mechanically strong perovskite-based solar cells, as required for commercialization.



In the past few years, monolithic perovskite/silicon tandems, combining perovskite and silicon solar cell technologies, have enabled high power conversion efficiencies (PCEs) in a possible cost-effective way, which holds great promise for their mass production.<sup>1–3</sup> To date, most of the tandem research has focused on pursuing PCE increases,<sup>4–9</sup> often by introducing sophisticated stacks of materials. However, for commercialization, tandems need to be integrated into solar panels, which may pose significant cell-to-module related technological challenges,<sup>10</sup> which urgently need to be identified and mitigated. Conventional monofacial single-junction crystalline silicon (c-Si) photovoltaic (PV) modules consist of a front glass sheet, strings of series-connected c-Si solar cells, sandwiched between two encapsulant layers (front and rear, at present usually made from ethylene vinyl acetate, EVA), and a polymeric backsheet.<sup>10,11</sup> This stack is then laminated by vacuum annealing to melt and solidify the encapsulant layers, which also aids in anchoring the strings of cells in the module. For module integration of perovskite/silicon tandem solar cells, this process should be altered. Indeed, due to the sensitivity of perovskites to moisture,<sup>12</sup> the backsheet needs to be replaced with a rear glass sheet, acting as

a more effective barrier; such glass/glass module technology is already well established for bifacial c-Si PV technology.<sup>11</sup> Moreover, classic module lamination tends to shrink the encapsulant layers upon solidification, which can be several centimeters over the module dimensions. We find this often to cause tandem-device delamination, resulting in catastrophic module failure. For lab-scale devices, this can be resolved by removing the encapsulant layers and sealing the glass/glass modules only at their edges, for instance with butyl-rubber derivatives.<sup>13–15</sup> However, for larger modules, the absence of encapsulants may compromise the anchoring and structural stability of the strings of fragile cells. Therefore, understanding and resolving tandem delamination is a key challenge toward its commercialization.<sup>16</sup> In 2018, Checharoen et al. reported on delamination of single-junction perovskite solar cells

Received: October 3, 2021

Accepted: December 30, 2021

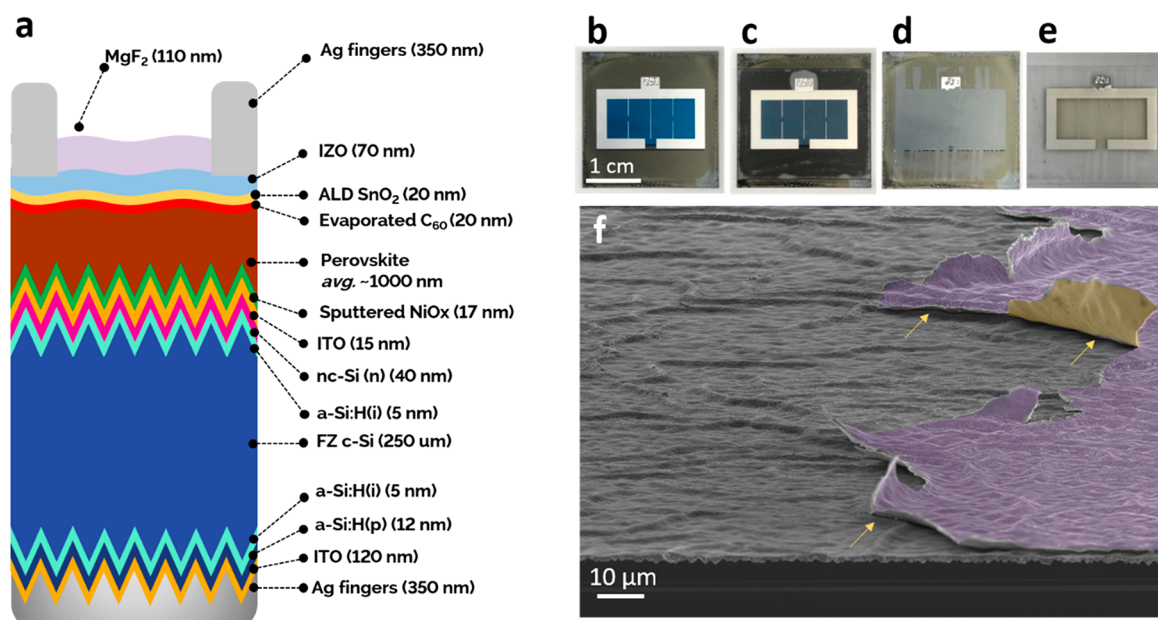


Figure 1. Delamination of the top electrode: (a) structure of the  $p$ - $i$ - $n$  tandem. (b) Picture of the tandem solar cell, (c) covered by tape, (d) after the peeling, with the emerging surface, and (e) peeled part left on the tape. (f) False-colored tilted SEM image of the peeled electrode. The peeled surface presents the typical wrinkles of the perovskite surface. The purple area represents the top of the Ag/MgF<sub>2</sub> electrode, while the yellow area the lift-off film that delaminated. The yellow arrows indicate the interface where delamination happens.

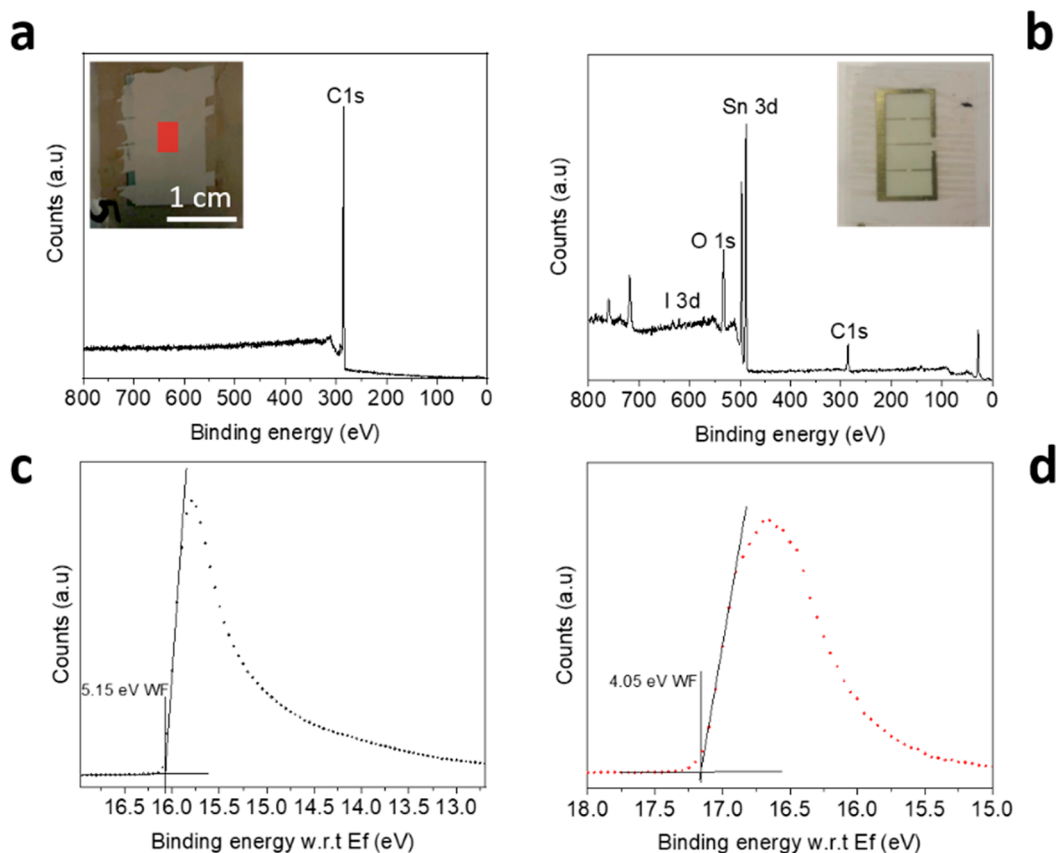
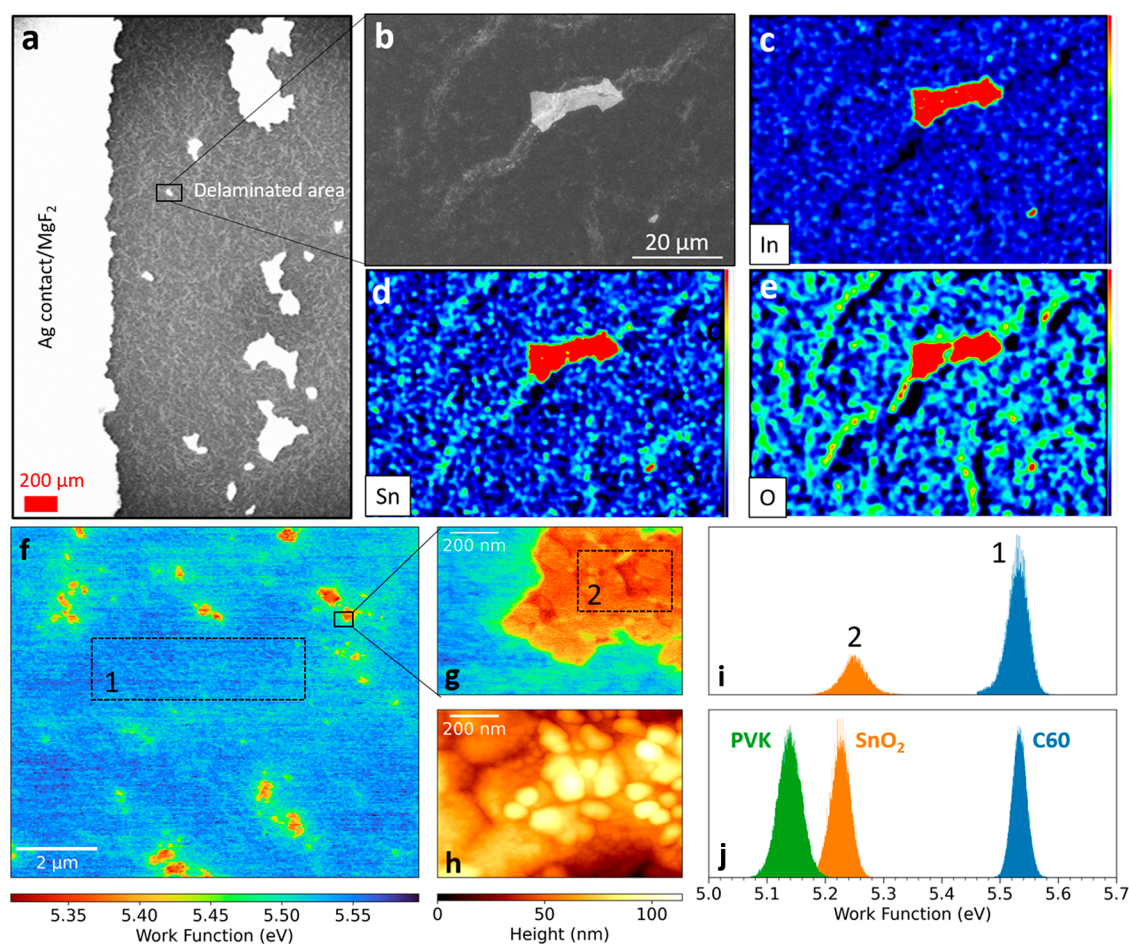


Figure 2. XPS survey of the peeled electrode. (a) XPS survey of the emerging surface. The inset is a picture of the delaminated sample. The red square represents the XPS probed area. (b) XPS survey of the peeled electrode. The inset represents the peeled electrode. (c) UPS spectrum of the emerging surface. (d) UPS spectrum of the peeled electrode.

59 (PSCs) in the  $p$ - $i$ - $n$  architecture, the same configuration as  
 60 most efficient perovskite/silicon tandems.<sup>13,14</sup> With double  
 61 cantilever beam experiments, they found that the delamination

occurs within the electron-selective contact, particularly in the  
 62 phenyl-C61-butyric acid methyl ester (PCBM) film. This film  
 63 features the lowest fracture energy among the whole device  
 64



**Figure 3.** Microscopic investigation of the delamination. (a) Large area overview SEM image at the edge of the peeled area. (b) Closer SEM top-view image of the investigated area. (c–e) EDX mapping of indium, tin, and oxygen, respectively. (f)  $10 \mu\text{m}^2$  KPFM map of a delaminated tandem solar cell. (g, h)  $1 \mu\text{m}^2$  close-up of one of the residuals as measured by KPFM and dynamic AFM morphology, respectively. (i) Work function distributions of regions 1 (blue) and 2 (orange), corresponding to the regions delimited by dashed rectangles in f) and g). (j) Work function distributions of calibration samples consisting of Si/ITO/Perovskite (green), Si/ITO/perovskite/ $\text{C}_{60}$  (blue), and Si/ITO/perovskite/ $\text{C}_{60}/\text{SnO}_2$  (orange).

65 stack, resulting in its rupture under stress.<sup>13,14</sup> Here, we  
 66 thoroughly investigate the nature of delamination mechanism  
 67 in state-of-the-art *p-i-n* tandems (Figure 1a) by intentionally  
 68 peeling-off the top electrode (Figure 1b–e). We found that,  
 69 the top electrode fully delaminates, even preserving the pristine  
 70 conductivity of the front transparent contact (Figure S1). For  
 71 improved understanding of the delamination process, we  
 72 collected tilted-angle scanning electron microscopy (SEM)  
 73 images at the peeling interface (Figure 1f). At the bottom of  
 74 the image, the typical textured surface of the c-Si bottom cell is  
 75 visibly covered by the perovskite layer. The perovskite exhibits  
 76 on its surface the characteristic wrinkles induced during the  
 77 crystallization process. These wrinkles are induced by the  
 78 presence of Cs in the perovskite formulation and the presence  
 79 of the textured substrate underneath.<sup>17</sup> The purple area  
 80 highlights the top part of the contact (the Ag finger is covered  
 81 by the  $\text{MgF}_2$  anti-reflective coating (ARC)) that is partially  
 82 lifted, while the yellow area represents the film that  
 83 delaminated.

84 To identify the nature of the layers that delaminate, we  
 85 investigated both exposed surfaces of the failed device  
 86 interface, with a combination of surface sensitive (1–10 nm)  
 87 X-ray and ultraviolet photoelectron spectroscopies (XPS/  
 88 UPS), energy dispersive X-ray analysis (EDX), and Kelvin

probe force microscopy (KPFM). Figure 2a shows the XPS  
 survey scan of the films present on the surface emerging from  
 the tandem (red square in the inset). The spectrum shows the  
 typical feature of carbon in the form of fullerene ( $\text{C}_{60}$ ), a single  
 $\text{C}1s$  peak, accompanied by characteristic shake-up satellite  
 features,<sup>18</sup> with traces of elements belonging to the perovskite,  
 but not of elements related to the contact (see Figure S2 for  
 more details). From the quantification of the peak areas, we  
 identified the material present on the tape (Figure 2b) as the  
 atomic layer deposited (ALD)  $\text{SnO}_2$  buffer layer (film  
 composition: Sn 24 At%, O 42 At%, C 33% and a trace of I  
 of 0.5%). To further investigate, we acquired UPS spectra of  
 both samples with a depth sensitivity of  $\sim 1$  nm. Figure 2c  
 shows the UPS spectrum of the surface emerging from the  
 tandem. The secondary electron cut-off (SECO) indicates a  
 work function (WF) of 5.15 eV, which matches well with that  
 of pristine  $\text{C}_{60}$  measured independently on a freshly evaporated  
 $\text{C}_{60}$  layer as well as resulting in an acceptable ionization energy  
 (IE) of 6.50 eV (calculated from  $\text{WF} + \text{VBM} - E_f$ ). Figure 2d  
 shows the SECO of the film present on the tape side. The  
 energy levels are univocally attributed to  $\text{SnO}_2$ , with a deep  
 valence band at  $-7.90$  eV (resulting in a WF of 4.05 eV).<sup>19,20</sup>  
 The UPS analysis confirms the finding of the XPS analysis,  
 suggesting that the delamination happened on a macroscopic

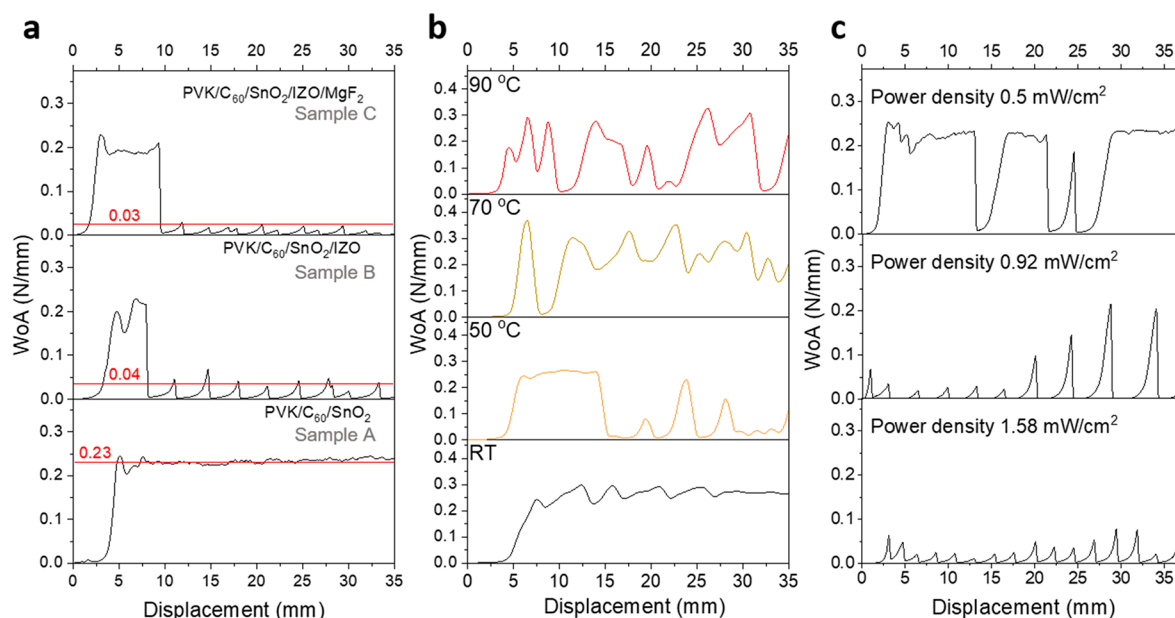


**Figure 4.** (a) 180-degree peel-off test for tandem test structures. PVK is the perovskite layer. Sample A (PVK/C<sub>60</sub>/SnO<sub>2</sub>); sample B (PVK/C<sub>60</sub>/SnO<sub>2</sub>/IZO); sample C (PVK/C<sub>60</sub>/SnO<sub>2</sub>/IZO/MgF<sub>2</sub>). The red line averages the adhesion energy in N/mm. (b) 180-degree peel-off test for three identical test structures: PVK/C<sub>60</sub>/SnO<sub>2</sub> annealed at different temperatures: RT black, 50 °C orange, 70 °C yellow, 90 °C red. (c) Peel-off tests for tandem structures with the IZO layer deposited with different powers. The sample labeled 0.92 mW/cm<sup>2</sup> is the reference deposition for tandem applications.

113 scale at the interface between the fullerene and the SnO<sub>2</sub> buffer  
114 layer, as evidenced by the area bulk averaging property of the  
115 techniques.

116 To understand the microscopic nature of the delamination  
117 we combined EDX topography with KPFM mapping. Figure  
118 3a shows a low-magnification SEM top view of the  
119 delaminated interface of the tandem; the white bright side  
120 represents the MgF<sub>2</sub> top layer, whereas the dark side is the  
121 emerging surface. With a closer look, we noticed that the  
122 delamination is not uniform. Indeed, we spotted several  
123 micrometer-sized areas where the top contact appears to be  
124 intact. Moreover, the morphology of the perovskite is not  
125 perfectly flat, and we noticed a difference in contrast on top of  
126 the wrinkles, induced by perovskite crystallization. Therefore,  
127 we performed EDX topography on one of those regions, where  
128 the top electrode overlaps on top of a wrinkle (Figure 3b). The  
129 EDX mapping of In, Sn, and O (Figure 3c–e) clearly shows  
130 that the bright area is part of the top electrode stack (which in  
131 this region consists of the ALD-SnO<sub>2</sub> buffer layer and indium  
132 zinc oxide (IZO) electrode) that did not delaminate with the  
133 rest of the film. Moreover, we noticed traces of Sn and O on  
134 top of the wrinkle, suggesting the presence of the SnO<sub>2</sub> buffer  
135 layer. This is of significant importance since the microscopic  
136 roughness of the materials can have a fundamental role in  
137 controlling the adhesion between the layers. To further  
138 investigate the microscopic nature of the delamination we  
139 took advantage of KPFM mapping in an argon ambient and in  
140 dark conditions, to avoid sample degradation during the  
141 measurement. Figure 3f shows a 10 μm<sup>2</sup> KPFM scan of a  
142 delaminated tandem solar cell. This map confirms the non-  
143 uniformity of the delamination at the micrometer scale, with  
144 clear presence of low WF residuals on top of a high WF  
145 substrate. Figure 3g,h shows a 1 μm<sup>2</sup> KPFM and morphology  
146 close-up of one of the residuals, respectively. We note the close  
147 correlation between the WF map and morphology, confirming  
148 that the micrometer-sized islands are residuals of a different

chemical species than the substrate. The morphology and  
149 phase maps of the delaminated solar cell are reported in Figure  
150 S3. Figure 3i shows the distribution of the WFs measured in  
151 regions 1 (substrate) and 2 (residual), as indicated in Figure 2f  
152 and 3g by dashed rectangles. To assess the nature of the two  
153 species, we measured WF distributions of calibration samples  
154 consisting of Si/ITO/perovskite, Si/ITO/perovskite/C<sub>60</sub>, and  
155 Si/ITO/perovskite/C<sub>60</sub>/SnO<sub>2</sub> structures, shown in Figure 3l as  
156 green, blue, and orange histograms, respectively. The KPFM  
157 and morphology maps of the calibration samples are reported  
158 in Figure S3. The WF values measured by KPFM on the  
159 reference samples match well the values obtained by UPS scans  
160 on the same samples, as shown in Figure S4. A comparison  
161 with the distribution of the delaminated solar cell unequivocally  
162 shows that the exposed layer consists of a C<sub>60</sub> film with  
163 SnO<sub>2</sub> residuals on top. 164

To better understand the delamination mechanism, we  
165 performed density functional theory simulations of the C<sub>60</sub>/166  
167 SnO<sub>2</sub> interface to model the adhesion between the two  
168 materials. Specifically, we studied various orientations of the  
169 C<sub>60</sub> molecule on the SnO-terminated (110) surface of SnO<sub>2</sub>.  
170 We found that the carbon atoms shared by pentagons and  
171 hexagons of the C<sub>60</sub> molecule interact with both the Sn and O  
172 atoms of the SnO<sub>2</sub> surface with a binding energy of −0.28 eV.  
173 The optimized structure is shown in Figure S5. The Bader  
174 charge analysis demonstrated a transfer of less than 0.02  
175 electrons from the C<sub>60</sub> molecule to the SnO<sub>2</sub> surface. Finally,  
176 we determined that the distance between the C<sub>60</sub> molecule and  
177 SnO<sub>2</sub> surface is 3.22 Å, falling into the physisorption range.  
178 With this information at hand, we then evaluated the fracture  
179 energy of the C<sub>60</sub>/SnO<sub>2</sub> interface, namely the work of adhesion  
180 (WoA), using 180° peel-off measurements (Figure 4a). To  
181 isolate the fracture, we realized different test structures on top  
182 of perovskite films that mimic the tandem architecture: C<sub>60</sub>/  
183 SnO<sub>2</sub> (sample A), C<sub>60</sub>/SnO<sub>2</sub>/IZO (sample B), and C<sub>60</sub>/SnO<sub>2</sub>/  
184 IZO/MgF<sub>2</sub> (sample C). Surprisingly, we found that the WoA

185 between the  $C_{60}$  and the  $SnO_2$  bilayer ( $\sim 0.23$  N/mm) is  
186 higher than that of the peeling tape interface ( $\sim 0.20$  N/mm,  
187 see Figure S6). Indeed, we did not notice any delamination on  
188 sample A. However, when the  $SnO_2$  is capped with a sputtered  
189 IZO layer as transparent electrode (sample B) we experienced  
190 the same delamination behavior of the tandem itself, fracturing  
191 at the  $C_{60}/SnO_2$  interface. Moreover, we noticed that the  
192 delamination happens via a slip-and-stick mechanism and, as  
193 expected, is accentuated in the presence of film edges (see  
194 Figure S7). From the delamination profile of sample B we  
195 evaluated a WoA of 0.04 N/mm. Next, we found that coating  
196 the IZO layer with an additional ARC layer of  $MgF_2$  (sample  
197 C) further reduces the WoA of the  $C_{60}/SnO_2$  interface (0.03  
198 N/mm). The  $MgF_2$  layer is adopted at the single-cell level to  
199 enhance the current response; it is not meant to be included at  
200 the module level, since the encapsulant features a similarly low  
201 refractive index. However, at the lab level and for practical  
202 purposes, tandem devices are often laminated with  $MgF_2$  either  
203 for stability or outdoor performance evaluation.<sup>4,21</sup> In our case,  
204 we found that the presence of  $MgF_2$  as second ARC is  
205 deteriorating the long-term stability of the device, as it  
206 enhances the possibility of delamination. However, the lower  
207 adhesion energy attributed to the presence of IZO or  $MgF_2$  is  
208 not due to the layers themselves, but rather to a weakening of  
209 the  $C_{60}/SnO_2$  interface during the IZO sputtering or  $MgF_2$   
210 thermal evaporation processes. Indeed, it is likely that during  
211 these depositions the sample heats up, particularly during the  
212  $MgF_2$  deposition (reaching temperature close to  $\sim 50$  °C). The  
213 higher temperature weakens the bonding between  $C_{60}$  and  
214  $SnO_2$ , favoring the delamination process. Therefore, to validate  
215 our hypothesis, we performed a second peel-off experiment  
216 (Figure 4b) with four identical test-structures of perovskite/  
217  $C_{60}/SnO_2$  but annealed at different temperatures (room  
218 temperature (RT) gray line, 50 °C orange line, 70 °C yellow  
219 line, and 90 °C red line). The outcome of the experiment  
220 validated our hypothesis. Indeed, the sample without annealing  
221 (RT) showed a pattern similar to sample A in Figure 4a in  
222 terms of profile and peeling force. On the contrary, a mild  
223 annealing at 50 °C (and consistently at higher temperatures)  
224 showed the clear features of delamination, as evidenced by the  
225 pictures of the samples in Figure S8. Lastly, we shifted our  
226 attention to the impact of the IZO deposition. The direct  
227 deposition of TCOs by radio frequency (rf) sputtering is  
228 known to possibly create damage in the underlying layers.<sup>22</sup>  
229 Even in silicon heterojunction solar cell manufacturing the  
230 TCO deposition is followed by an annealing step to recover  
231 the damage done to the amorphous silicon contact layers  
232 during such sputtering. In perovskite/silicon tandems, the  
233  $SnO_2$  buffer layer protects the soft fullerene and perovskite  
234 layers from the deposition of IZO. Figure 4a shows a clear  
235 difference between sample A and B, suggesting that the IZO  
236 deposition affects the WoA. Therefore, we deposited IZO  
237 layers with different power densities: 0.5, 0.92, and 1.58 mW/  
238  $cm^2$ , which represent soft deposition, our baseline deposition,  
239 and a faster deposition conditions, respectively (all the films  
240 share the same IZO thickness). Figure 4c shows the WoA  
241 profiles for the three samples. We noted that there is a  
242 correlation between the deposition power and the interfacial  
243 mechanical properties. Indeed, at higher power the samples  
244 delaminate easier, showing a lower WoA. To validate our  
245 findings, we performed a statistical analysis over a batch of six  
246 samples. Then we determined the average energy per sample  
247 by integrating the WoA (Figure S9). The distribution clearly

shows that the deposition of the IZO plays a key role in the  
delamination and suggests that a precise control of the  
deposition conditions is strategic to prevent this issue.

Few works in the past addressed delamination in PSCs.  
Cheacharoen et al., investigated this problem at the single-  
junction level and proposed the fracture of the PCBM layer, a  
functionalized version of  $C_{60}$ , as the origin.<sup>13,14</sup> Here we  
propose that the delamination originates at the  $C_{60}/SnO_2$   
interface with a neat separation of the two films at the  
macroscopic level, but influenced by the perovskite roughness  
at the microscopic level. Yet, in both cases, it is clear that the  
presence of the fullerene (or its derivatives) poses a serious  
roadblock toward the development of mechanically stable  
perovskite-based solar cells. Indeed, the challenge is not limited  
to the fabrication of modules, but also to the stability of the  
performances. In real applications, the temperature of the  
tandems can reach up to 50–60 °C at the peak-sun hours.<sup>1,23</sup>  
The periodic temperature changes typical for outdoor  
performance impose cyclic stresses to the materials, in  
particular to those that have different thermal expansion  
coefficients. Therefore, it is of high urgency to address the  
delamination issue at the widely used  $C_{60}$  interface within the  
perovskite community.

Fullerene-based n-type contacts are an iconic part of *p-i-n*  
PSCs,<sup>24</sup> in particular thanks to their unique property in  
reducing the hysteresis in the current–voltage character-  
istic.<sup>25,26</sup> Currently, there are no reasonable candidates that can  
be used in this polarity configuration as an alternative to  
fullerenes without losing performance, stability, or exacerbating  
hysteresis.<sup>27</sup> Therefore, the best approach for *p-i-n* PSCs to  
address delamination is the functionalization of the fullerene  
and its surface.<sup>28</sup> In this direction, in tandems, particular  
attention should be given toward the realization of a strong  
chemical bond between the  $C_{60}$  and the buffer layer (inserted  
between  $C_{60}$  layer and sputtered transparent top electrode), to  
enable a proper lamination of stable perovskite/silicon  
tandems. This bond can be enhanced either with an *in situ*  
approach or with other layers deposited on top of the fullerene.  
In both cases, the treatment must respect the perovskite  
constraints, in terms of solvent compatibility and temperature  
processing. In parallel, particular attention should be given to  
preserve the electronic properties of the ETL and to avoid  
parasitic absorption that can affect the current output of the  
tandem. Lastly, we proved that the processing conditions for  
the tandem fabrication have a significant role in delamination.  
Temperature treatments or post-annealing treatments neg-  
atively affect the weak adhesion between  $C_{60}$  and  $SnO_2$  and  
they should be minimized or avoided completely. Moreover,  
the impact of the sputtering process should be reduced for  
example employing soft-landing depositions such as the hollow  
cathode technique and the parallel sputtering configuration.

In this work, we showed the origin of the delamination in  
perovskite/silicon tandem solar cells. Delamination is among  
the most serious concerns for the manufacturing of tandem  
modules and for the stability of the tandem performances, yet  
hardly discussed to date. Contrarily to what has been reported  
earlier for single-junction PSCs, we found that delamination  
happens at the interface between the  $C_{60}$  extraction layer and  
the  $SnO_2$  buffer layer. Moreover, we realized that the adhesion  
between the two layers is influenced by the perovskite  
morphology; indeed, the wrinkles induced during the perov-  
skite crystallization retain microscopically the adhesion  
between the  $C_{60}$  and  $SnO_2$ . This provides the opportunity in

311 the near future to engineer the roughness of the perovskite  
312 layer in such a way that the probability for delamination to  
313 occur is reduced. Furthermore, we showed that the temper-  
314 ature during the processing of the tandem has an influence on  
315 the adhesion between the  $C_{60}$  and  $SnO_2$ . Such an under-  
316 standing is pivotal to improve the tandem fabrication, toward  
317 more stable performances.

## 318 ■ ASSOCIATED CONTENT

### 319 ■ Supporting Information

320 The Supporting Information is available free of charge at  
321 <https://pubs.acs.org/doi/10.1021/acsenergylett.1c02148>.

322 Experimental section; peeling of the top electrode; XPS  
323 spectra after the peeling of the electrode; morphology  
324 and KPFM maps; work function comparison; DFT  
325 calculations; work of adhesion calibration and stick-and-  
326 slip behavior; effect of temperature on the delamination;  
327 statistic distribution of the work of adhesion as a  
328 function of the IZO sputtering power (PDF)

329 Video showing the  $180^\circ$  stick-and-slip behavior (MP4)

## 330 ■ AUTHOR INFORMATION

### 331 Corresponding Authors

332 Michele De Bastiani – KAUST Solar Center (KSC), Physical  
333 Sciences and Engineering Division (PSE), King Abdullah  
334 University of Science and Technology (KAUST), Thuwal  
335 23955-6900, Kingdom of Saudi Arabia; [orcid.org/0000-0002-4870-2699](https://orcid.org/0000-0002-4870-2699); Email: [michele.debastiani@kaust.edu.sa](mailto:michele.debastiani@kaust.edu.sa)

337 Stefaan De Wolf – KAUST Solar Center (KSC), Physical  
338 Sciences and Engineering Division (PSE), King Abdullah  
339 University of Science and Technology (KAUST), Thuwal  
340 23955-6900, Kingdom of Saudi Arabia; [orcid.org/0000-0003-1619-9061](https://orcid.org/0000-0003-1619-9061); Email: [stefaan.dewolf@kaust.edu.sa](mailto:stefaan.dewolf@kaust.edu.sa)

### 342 Authors

343 Giovanni Armaroli – Department of Physics and Astronomy,  
344 University of Bologna, 40127 Bologna, Italy

345 Rawan Jalmoed – KAUST Solar Center (KSC), Physical  
346 Sciences and Engineering Division (PSE), King Abdullah  
347 University of Science and Technology (KAUST), Thuwal  
348 23955-6900, Kingdom of Saudi Arabia

349 Laura Ferlauto – Department of Physics and Astronomy,  
350 University of Bologna, 40127 Bologna, Italy;  
351 Interdepartmental Center for Industrial Research of the  
352 University of Bologna (CIRI-MAM), 40136 Bologna, Italy;  
353 [orcid.org/0000-0003-2131-6795](https://orcid.org/0000-0003-2131-6795)

354 Xiaole Li – King Abdullah University of Science and  
355 Technology (KAUST), Physical Science and Engineering  
356 Division, Mechanics of Composites for Energy and Mobility  
357 Lab., Thuwal 23955-6900, Saudi Arabia

358 Ran Tao – King Abdullah University of Science and  
359 Technology (KAUST), Physical Science and Engineering  
360 Division, Mechanics of Composites for Energy and Mobility  
361 Lab., Thuwal 23955-6900, Saudi Arabia

362 George T. Harrison – KAUST Solar Center (KSC), Physical  
363 Sciences and Engineering Division (PSE), King Abdullah  
364 University of Science and Technology (KAUST), Thuwal  
365 23955-6900, Kingdom of Saudi Arabia

366 Mathan K. Eswaran – KAUST Solar Center (KSC), Physical  
367 Sciences and Engineering Division (PSE), King Abdullah  
368 University of Science and Technology (KAUST), Thuwal  
369 23955-6900, Kingdom of Saudi Arabia

Randi Azmi – KAUST Solar Center (KSC), Physical Sciences  
and Engineering Division (PSE), King Abdullah University of  
Science and Technology (KAUST), Thuwal 23955-6900,  
Kingdom of Saudi Arabia

Maxime Babics – KAUST Solar Center (KSC), Physical  
Sciences and Engineering Division (PSE), King Abdullah  
University of Science and Technology (KAUST), Thuwal  
23955-6900, Kingdom of Saudi Arabia

Anand S. Subbiah – KAUST Solar Center (KSC), Physical  
Sciences and Engineering Division (PSE), King Abdullah  
University of Science and Technology (KAUST), Thuwal  
23955-6900, Kingdom of Saudi Arabia; [orcid.org/0000-0002-7505-3209](https://orcid.org/0000-0002-7505-3209)

Erkan Aydin – KAUST Solar Center (KSC), Physical Sciences  
and Engineering Division (PSE), King Abdullah University of  
Science and Technology (KAUST), Thuwal 23955-6900,  
Kingdom of Saudi Arabia; [orcid.org/0000-0002-8849-2788](https://orcid.org/0000-0002-8849-2788)

Thomas G. Allen – KAUST Solar Center (KSC), Physical  
Sciences and Engineering Division (PSE), King Abdullah  
University of Science and Technology (KAUST), Thuwal  
23955-6900, Kingdom of Saudi Arabia

Craig Combe – KAUST Solar Center (KSC), Physical  
Sciences and Engineering Division (PSE), King Abdullah  
University of Science and Technology (KAUST), Thuwal  
23955-6900, Kingdom of Saudi Arabia

Tobias Cramer – Department of Physics and Astronomy,  
University of Bologna, 40127 Bologna, Italy; [orcid.org/0000-0002-5993-3388](https://orcid.org/0000-0002-5993-3388)

Derya Baran – KAUST Solar Center (KSC), Physical Sciences  
and Engineering Division (PSE), King Abdullah University of  
Science and Technology (KAUST), Thuwal 23955-6900,  
Kingdom of Saudi Arabia; [orcid.org/0000-0003-2196-8187](https://orcid.org/0000-0003-2196-8187)

Udo Schwingenschlögl – KAUST Solar Center (KSC),  
Physical Sciences and Engineering Division (PSE), King  
Abdullah University of Science and Technology (KAUST),  
Thuwal 23955-6900, Kingdom of Saudi Arabia; [orcid.org/0000-0003-4179-7231](https://orcid.org/0000-0003-4179-7231)

Gilles Lubineau – King Abdullah University of Science and  
Technology (KAUST), Physical Science and Engineering  
Division, Mechanics of Composites for Energy and Mobility  
Lab., Thuwal 23955-6900, Saudi Arabia; [orcid.org/0000-0002-7370-6093](https://orcid.org/0000-0002-7370-6093)

Daniela Cavalcoli – Department of Physics and Astronomy,  
University of Bologna, 40127 Bologna, Italy; [orcid.org/0000-0002-2417-1248](https://orcid.org/0000-0002-2417-1248)

Complete contact information is available at:  
<https://pubs.acs.org/doi/10.1021/acsenergylett.1c02148>

## Notes

The authors declare no competing financial interest.

## ACKNOWLEDGMENTS

This work was supported by the King Abdullah University of  
Science and Technology (KAUST) Office of Sponsored  
Research (OSR) under award nos. KAUST OSR-2018-  
CARF/CCF-3079, KAUST OSR-CRG RF/1/3383, KAUST  
OSR-CRG2018-3737, and IED OSR-2019-4208. L.F. and D.C.  
acknowledge funding from the European Community through  
the POR-FESR “FORTRESS” project, grant no. 427  
I38D18000150009 (PG/2018/629121).



## 430 ■ REFERENCES

- 431 (1) Aydin, E.; et al. Interplay between temperature and bandgap  
432 energies on the outdoor performance of perovskite/silicon tandem  
433 solar cells. *Nature Energy* **2020**, *5*, 851–859.
- 434 (2) Al-Ashouri, A.; et al. Monolithic perovskite/silicon tandem solar  
435 cell with > 29% efficiency by enhanced hole extraction. *Science* **2020**,  
436 *370*, 1300–1309.
- 437 (3) Köhnen, E.; et al. 27.9% Efficient Monolithic Perovskite/Silicon  
438 Tandem Solar Cells on Industry Compatible Bottom Cells. *Solar RRL*  
439 **2021**, *5*, 2100244.
- 440 (4) De Bastiani, M.; et al. Efficient bifacial monolithic perovskite/  
441 silicon tandem solar cells via bandgap engineering. *Nature Energy*  
442 **2021**, *6*, 167.
- 443 (5) Isikgor, F. H.; et al. Concurrent cationic and anionic perovskite  
444 defect passivation enables 27.4% perovskite/silicon tandems with  
445 suppression of halide segregation. *Joule* **2021**, *5*, 1566–1586.
- 446 (6) Aydin, E.; et al. Ligand-bridged charge extraction and enhanced  
447 quantum efficiency enable efficient n-i-p perovskite/silicon tandem  
448 solar cells. *Energy Environ. Sci.* **2021**, *14*, 4377.
- 449 (7) Hou, Y.; et al. Efficient tandem solar cells with solution-  
450 processed perovskite on textured crystalline silicon. *Science* **2020**, *367*,  
451 1135–1140.
- 452 (8) Xu, J.; et al. Triple-halide wide-band gap perovskites with  
453 suppressed phase segregation for efficient tandems. *Science* **2020**, *367*,  
454 1097–1104.
- 455 (9) Kim, D.; et al. Efficient, stable silicon tandem cells enabled by  
456 anion-engineered wide-bandgap perovskites. *Science* **2020**, *368*, 155–  
457 160.
- 458 (10) De Bastiani, M.; et al. All Set for Efficient and Reliable  
459 Perovskite/Silicon Tandem Photovoltaic Modules? *Solar RRL* **2021**,  
460 *5*, 2100493.
- 461 (11) Kopecek, R.; Libal, J. Bifacial Photovoltaics 2021: Status,  
462 Opportunities and Challenges. *Energies* **2021**, *14*, 2076.
- 463 (12) Ugur, E.; et al. How Humidity and Light Exposure Change the  
464 Photophysics of Metal Halide Perovskite Solar Cells. *Solar RRL* **2020**,  
465 *4*, 2000382.
- 466 (13) Checharoen, R.; et al. Encapsulating perovskite solar cells to  
467 withstand damp heat and thermal cycling. *Sustainable Energy & Fuels*  
468 **2018**, *2*, 2398–2406.
- 469 (14) Checharoen, R.; et al. Design and understanding of  
470 encapsulated perovskite solar cells to withstand temperature cycling.  
471 *Energy Environ. Sci.* **2018**, *11*, 144–150.
- 472 (15) Shi, L.; et al. Gas chromatography–mass spectrometry analyses  
473 of encapsulated stable perovskite solar cells. *Science* **2020**, *368* (6497),  
474 aba2412.
- 475 (16) Rolston, N.; et al. Mechanical integrity of solution-processed  
476 perovskite solar cells. *Extreme Mechanics Letters* **2016**, *9*, 353–358.
- 477 (17) Bush, K. A.; et al. Controlling thin-film stress and wrinkling  
478 during perovskite film formation. *ACS Energy Letters* **2018**, *3*, 1225–  
479 1232.
- 480 (18) Liu, H.; Taheri, B.; Jia, W. Anomalous optical response of C 60  
481 and C 70 in toluene. *Phys. Rev. B* **1994**, *49*, 10166.
- 482 (19) Kuang, Y.; et al. Low-temperature plasma-assisted atomic-layer-  
483 deposited SnO<sub>2</sub> as an electron transport layer in planar Perovskite  
484 solar cells. *ACS Appl. Mater. Interfaces* **2018**, *10*, 30367–30378.
- 485 (20) Dong, Q.; et al. Interpenetrating interfaces for efficient  
486 perovskite solar cells with high operational stability and mechanical  
487 robustness. *Nat. Commun.* **2021**, *12*, 6484.
- 488 (21) De Bastiani, M.; et al. Toward Stable Monolithic Perovskite/  
489 Silicon Tandem Photovoltaics: A Six-Month Outdoor Performance  
490 Study in a Hot and Humid Climate. *ACS Energy Lett.* **2021**, *6*, 2944–  
491 2951.
- 492 (22) Aydin, E.; et al. Sputtered transparent electrodes for  
493 optoelectronic devices: Induced damage and mitigation strategies.  
494 *Matter* **2021**, *4*, 3549–3584.
- 495 (23) Tress, W.; et al. Performance of perovskite solar cells under  
496 simulated temperature-illumination real-world operating conditions.  
497 *Nature energy* **2019**, *4*, 568–574.
- (24) Docampo, P.; Ball, J. M.; Darwich, M.; Eperon, G. E.; Snaith, 498  
H. J. Efficient organometal trihalide perovskite planar-heterojunction 499  
solar cells on flexible polymer substrates. *Nat. Commun.* **2013**, *4*, 500  
2761. 501
- (25) Shao, Y.; Xiao, Z.; Bi, C.; Yuan, Y.; Huang, J. Origin and 502  
elimination of photocurrent hysteresis by fullerene passivation in CH 503  
3 NH 3 Pbl 3 planar heterojunction solar cells. *Nat. Commun.* **2014**, 504  
*5*, 5784. 505
- (26) De Bastiani, M.; et al. Ion migration and the role of 506  
preconditioning cycles in the stabilization of the J–V characteristics 507  
of inverted hybrid perovskite solar cells. *Adv. Energy Mater.* **2016**, *6*, 508  
1501453. 509
- (27) Kim, S. S.; Bae, S.; Jo, W. H. A perylene diimide-based non- 510  
fullerene acceptor as an electron transporting material for inverted 511  
perovskite solar cells. *RSC Adv.* **2016**, *6*, 19923–19927. 512
- (28) Olah, G. A.; Bucsi, I.; Aniszfeld, R.; Prakash, G. S. Chemical 513  
reactivity and functionalization of C60 and C70 fullerenes. *Carbon* 514  
**1992**, *30*, 1203–1211. 515